Low Temperature Physics/Fizika Nizkikh Temperatur, 2020, v. 46, No. 4, pp. 441–448

Magnetic flux avalanches in Nb/NbN thin films

L.B.L.G. Pinheiro[1,2], M. Caputo[3,4], C. Cirillo[3,4], C. Attanasio[4,3], T.H. Johansen[5], W.A. Ortiz[2], A.V. Silhanek[6], and M. Motta[2]

[1]*Instituto Federal de São Paulo, Campus São Carlos, 13565-905 São Carlos, SP, Brazil*
E-mail: m.motta@df.ufscar.br

[2]*Departamento de Física, Universidade Federal de São Carlos, 13565-905 São Carlos, SP, Brazil*

[3]*CNR-SPIN, c/o Università degli Studi di Salerno, I-84084 Fisciano (Sa), Italy*

[4]*Dipartimento di Fisica "E.R. Caianiello", Università degli Studi di Salerno, FI-84084 Fisciano (Sa), Italy*

[5]*Department of Physics, University of Oslo, POB 1048, Blindern, 0316 Oslo, Norway.*

[6]*Experimental Physics of Nanostructured Materials, Q-MAT, CESAM, Université de Liège B-4000 Sart Tilman, Liège, Belgium*

Received November 25, 2019, published online February 28, 2020

Technological applications of NbN thin films may be threatened by the development of magnetic flux avalanches of thermomagnetic origin appearing in a large portion of the superconducting phase. In this work, we describe an approach to substantially suppress the magnetic flux avalanche regime, without compromising the upper critical field. This procedure consists of depositing a thin Nb layer before the reactive deposition of NbN, thus forming a bi-layered system. We use ac susceptibility and dc magnetometry to characterize both the single-layer films, Nb and NbN, and the bi-layered specimen, as well as calibrated magneto-optical imaging to map the instability regime of the studied samples. Magnetic flux imaging reveals interesting features of the dendritic flux avalanches in the bi-layer system, including halo-like patterns and crossing avalanches.

Keywords: Bi-layer, proximity effect, anti-avalanches, halo-like structure, crossing avalanches.

1. Introduction

According to the Bardeen–Stephen model [1], moving flux quanta dissipate energy due to the existence of an electric field through the normal core of each flux tube. The electric field accelerates the quasiparticles at the core thereby increasing their energy. This energy raising process is normally compensated by the energy relaxation rate of quasiparticles by means of their inelastic scattering [2]. Larkin and Ovchinnikov [3] realized that at high vortex velocities and correspondingly to high electric fields, the energy of quasiparticles can reach the superconducting gap, and diffuse into the superconducting phase surrounding the vortex core. As a consequence, the quasiparticle density in the vortex core is reduced and the vortex shrinks. The higher the vortex speed, the larger the deficit of quasiparticles at the core, the smaller its size and therefore the lower the damping coefficient η. If η decreases with increasing v, an instability point in the viscous flux flow is reached when the damping force $\eta(v)v$ starts to decline as v increases. A single vortex moving at such high velocities will then leave a wake of quasiparticles behind its path which can be regarded as a trail of depleted order parameter. Naturally, other moving vortices will find energetically favorable to follow the same path, and therefore a rearrangement of the Abrikosov vortex lattice is expected [4]. Eventually, these rivers of rapidly moving vortices, directly observed in Refs. 5 and 6, can transform into a phase slip line [7]. Note that the mechanism described above involves a non-thermal change of the distribution function of quasiparticles trapped in the vortex cores. Bezuglyj and co-authors [8,9] theoretically demonstrated that for magnetic fields above a certain threshold, the Larkin–Ovchinnikov instability switches to a pure thermal instability of flux flow resulting from the heating of quasiparticles.

The scenario described above corresponds to a bulk three-dimensional superconductor. When treating thin film geometries, where the penetration depth λ is larger than the thichness d of the film, an additional complication arises due to the fact that magnetic flux diffusion becomes strongly nonlocal and the vortex interaction is, to a large extent, mediated by the magnetic stray field and the screen-

ing of the in-plane supercurrents [10]. In this case, fastly moving flux quanta triggered either by a bias current [11,12] or by magnetic field changes [13] will then act as precursors of thermomagnetic flux avalanches [14].

These events consist of abrupt bursts of magnetic flux rushing into the sample, usually taking the form of dendrite-like structures. Their branches avoid each other during their growth [15], as reported both in experiments and in simulations using the thermomagnetic (TM) model [16,17]. This model describes the TM instabilities as the source of the flux avalanches, and predicts the existence of a threshold flux penetration depth (l^*) needed to trigger them. Once the penetration depth reaches l^*, the first burst takes place and the instability regime lasts until l^* is equal to half of the sample size [18–20]. Therefore, an upper and lower threshold fields [20] can be identified as the borders of the instability region for an isothermal field ramping. By means of magnetization measurements, Colauto *et al*. [21] were able to delineate a region on the magnetic field-temperature diagram where instabilities occur in a 200 nm thick Nb film. Among other materials, dendritic flux avalanches were also observed in NbN films, spanning over a large window of fields and temperatures [22].

Niobium nitride has higher critical field ($H_{c2}(T)$) and critical temperature (T_c) than pure Nb [23], what makes it NbN more suitable for superconducting devices [24], such as hot-electron bolometers [25], high-frequency superconducting circuits [26,27], single-photon detectors [28], and qubits for quantum computers [29], to name a few. Some applications may suffer from unwanted TM instabilities. Yurchenko *et al*. [30] have shown that such abrupt phenomena can be prevented by covering the NbN film with a copper coating. Independently, the idea of depositing a superconducting coating to enhance the applicability range was investigated in references [31–33]. In these works, it was shown that the stability improvement in superconducting wires covered by a thin superconductor depends on the electrical and thermal properties of both. Such a system becomes more stable if the capping layer has lower critical current density and higher heat capacity. Moreover, Ivry and co-workers [34] have proposed to use a thin proximities bi-layer structure NbN/WSi to optimize the performance of superconducting single-photon detectors.

Stacks of overlapping but electrically disconnected superconducting thin films is another way to affect the avalanche regimes, as demonstrated by Tamegai *et al*. [35]. They studied the critical states and thermomagnetic avalanche activities in three-dimensional nanostructured superconductors, i.e., stacks of Nb strips, insulated from each other by SiO_2 layers. Here, it was shown that flux avalanches can start in one layer and end at another. Although the avalanche activity has been shown to be reduced in superconducting films capped with a normal metal [30,36], thermomagnetic instabilities were not reported so far in bi-layered systems where NbN is in intimate contact with other superconducting layer. In this context, we present in this paper an approach capable of enhancing the potential applicability of NbN thin films by systematically exploring the avalanche regime in a bi-layer system composed of Nb and NbN thin films.

2. Experimental details

In order to perform a comparative analysis of the magnetic flux avalanche regime, 15 nm thick Nb (Nb15) and 60 nm thick NbN (NbN60) single films and hybrids (NbN/Nb) were deposited on Si(100) substrates at room temperature in a UHV DC diode magnetron sputtering system with a base pressure in the low of 10^{-8} mbar range. The Ar pressure, during the deposition of the Nb layer, was $P_{Ar} = 2.5\cdot10^{-3}$ mbar, while NbN was reactively sputtered in an atmosphere of Ar and N_2, with $P_{Ar} = 2.5\cdot10^{-3}$ mbar and $P_{N_2} = 0.7\cdot10^{-3}$ mbar. The deposition rates were $r_{Nb} = 0.26$ nm/s for Nb and $r_{NbN} = 0.17$ nm/s for NbN, as measured by a quartz crystal monitor previously calibrated by measuring the step height of photolithographically patterned films with a Bruker DektakXT stylus profiler. Samples with different structures were deposited by keeping the thickness of the Nb and NbN individual layers constant, namely $d_{Nb} = 15$ nm and $d_{NbN} = 60$ nm.

All the studied samples, having approximately the same area of 4×4 mm^2, were characterized by ac susceptometry and dc magnetometry in a commercial MPMS 5 Quantum Design magnetometer. Magneto-optical imaging (MOI) experiments, based on the Faraday effect [37], was carried out by placing a $Bi_xY_{1-x}FeO$ indicator [38] on top of the superconducting film. More details about the MOI setup can be found elsewhere [39,40]. In all measurements, the field H was applied perpendicular to the film surface. We also performed a numerical conversion from pixel intensity of magneto-optical (MO) images to the local magnetic flux density (B), mapping B_z all over the sample and its neighborhood, following the protocol reported in Ref. 41.

3. Results and discussion

3.1. Upper critical field

The critical temperature of superconducting thin films is thickness dependent and usually lower than the bulk values [42]. The onset critical temperature (T_c) of the samples were determined by ac susceptibility measurements, presented in Fig. 1(a), showing the following values: (6.90 ± 0.05) K for Nb15; (10.50 ± 0.05) K for the NbN60, and (10.00 ± 0.05) K for the hybrid sample. The critical temperature for the NbN film is close to values reported in the literature for similar thicknesses [43,44]. It is also important to mention that T_c of the single NbN layer is 0.5 K above of that the bi-layer, which is assumed here to be a consequence of growing the NbN film on top of the Nb layer already deposited on the substrate.

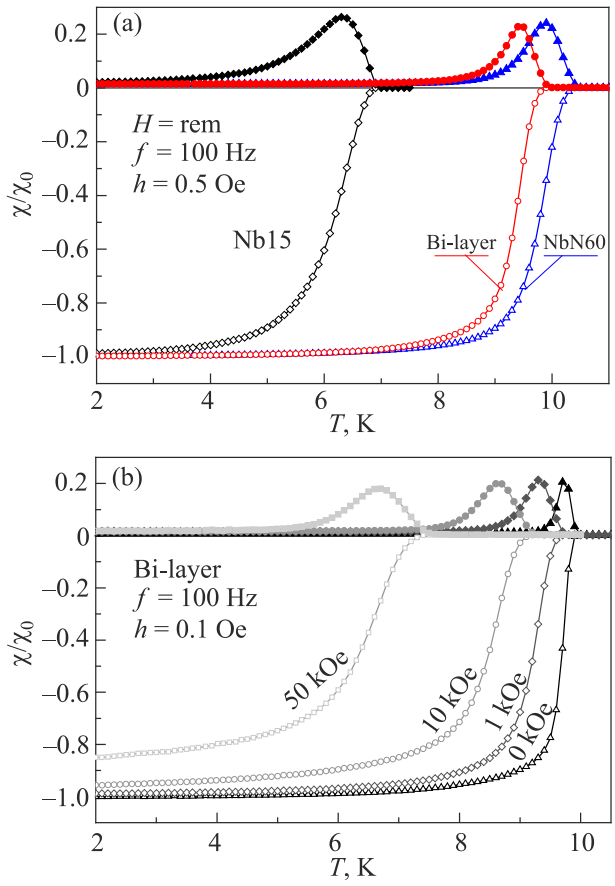

Fig. 1. ac susceptibility vs temperature for all investigated films (a) and for different applied magnetic fields H for the bi-layer system (b). The y axis is normalized by χ_0, which is the Meissner plateau value for the in-phase component of the ac susceptibility for each sample. The frequency (f) and the amplitude (h) of the ac excitation are indicated in each panel.

The fact that we do not observe a double or a broader transition in the bi-layer with respect to the single-layer films is a relevant hint suggesting highly transparent proximity effect [45] in between the layers. The absence of a double transition in the bi-layer sample remains for applied magnetic fields up to $H = 50$ kOe, as shown in Fig. 1(b). The existence of the proximity effect in the bi-layer specimen was also confirmed by a double transition in a sample with an additional 5 nm thick Nb_2O_5 insulating layer between the superconducting films (data not shown here).

By performing susceptibility measurements as a function of temperature for H up to 50 kOe, we determined the H_{c2} *vs* t diagram presented in Fig. 2, t being the reduced temperature, $t = T/T_c$. We estimate the $H_{c2}(0)$ values by fitting to the data the expression $H_{c2}(t) = H_{c2}(0)\cdot(1-t^2)$, plotted as dashed lines in the same graph. For both the bi-layer and NbN60 films, $H_{c2}(0)$ is close to 110 kOe, whereas for the Nb15 film it is approximately 27 kOe. Based on the derivative of the upper critical field versus temperature near T_c, we determined the superconducting

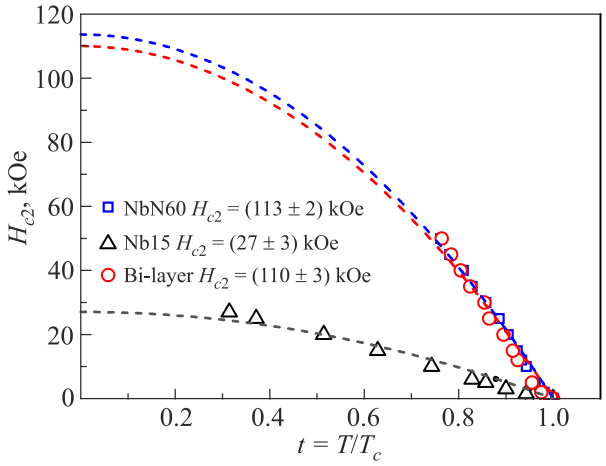

Fig. 2. H_{c2} vs reduced temperature $t = T/T_c$ for Nb15, NbN60, and the bi-layer, showing the extrapolated upper critical field at $T = 0$ K.

coherence lengths at 0 K ($\xi(0)$) of 10.7 nm, 4.7 nm, and 4.6 nm, for Nb15, NbN60, and the bi-layer, respectively. We did not detect flux avalanches in ac susceptibility measurements using driving fields up to 3.8 Oe, consistently with the existing literature [46,47], since avalanches occur only at higher fields.

3.2. Flux jumps regime

In order to identify the instability regimes of these systems, we measured the dc magnetization as a function of the applied magnetic field at the same reduced temperature $t = 0.3$. The result is presented in Fig. 3. The presence of magnetic flux jumps is clearly identified, for all samples as a noisy magnetic response, being particularly prominent for the NbN sample. Note, however, that avalanche activity is strongly suppressed by the proximities Nb layer (bi-layer sample).

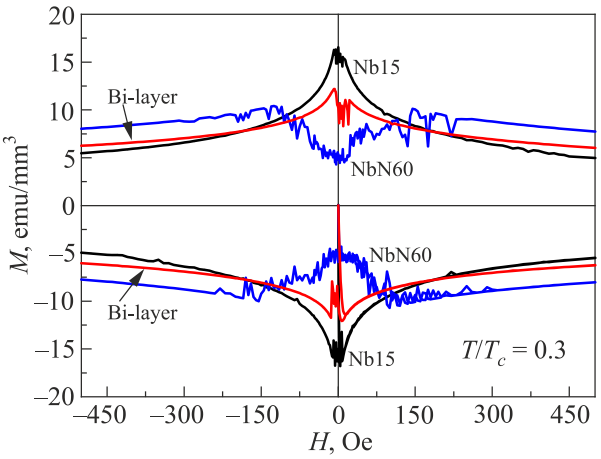

Fig. 3. dc magnetization as a function of the applied magnetic field at $t = \dfrac{T}{T_c} = 0.3$. The noisy response at low fields observed in all samples corresponds to the presence of magnetic flux jumps.

The critical current density (J_c) is a crucial parameter determining whether the thermomagnetic avalanches will take place [48]. The higher the J_c the larger the probability of observing flux jumps. Based on the Bean critical state model [49], one can roughly estimate J_c by the difference between the increasing and decreasing branches of the magnetization loop. This approach is acceptable in the smooth part of the magnetization loop (i.e., without flux jumps). A direct inspection of Fig. 3 shows that the critical current densities are rather similar for all samples, whereas the avalanche activity in the bi-layer sample has decreased as compared to that in the NbN single layer.

3.3. Magneto-optical imaging

Flux avalanches disrupting the smooth penetration after a zero-field cooling (ZFC) procedure can be visualized in the MO images of Fig. 4(a), for each of the investigated films. In all those MO images, the brighter the pixel, the higher perpendicular flux density. While large dendritic flux avalanches are observed in both NbN60 and Nb15 films, the bi-layer system exhibits much less activity, only some small finger-like avalanches occurring from the left and right edges. By changing the temperature, magnetization loops allow one to delineate the instability region in the applied magnetic field versus reduced temperature *H–t* diagram shown in Fig. 4(b). This figure presents one of the main messages from this work, namely a substantial enlargement of the stability regime, i.e., where only smooth flux penetration occurs, of the bi-layer system as compared to the bare NbN film. In other words, the bi-layer instability regime (in green) shrinks toward that of the Nb15 one (in yellow).

When $t \approx 0.5$, the NbN60 sample exhibits avalanches, as presented in the top MO image in Fig. 4(c). Both the bi-layer and the Nb15 films show smooth penetration, with the latter one in the full flux penetrated state. All the flux avalanches presented in Fig. 4 show positive flux only, i.e., they were created following the virgin curve of the magnetization loop by increasing the applied field from zero. By decreasing the applied magnetic field in a superconducting film, after keeping flux trapped into the sample, negative field-polarity avalanches, or simply anti-avalanches, can occur. Anti-avalanches can show an annihilation zone [15,50], i.e., a boundary of zero flux density separating the regions of flux and antiflux, which coexists due to the application of moderate reverse fields in a sample with flux already trapped by the pinning centers. This terminology has been used to describe the contour of anti-avalanches in the early stage of MO investigations of the abrupt flux penetration in superconducting thin films [15].

Once anti-avalanches are created by decreasing the applied magnetic field, their onset depends on the previous magnetic

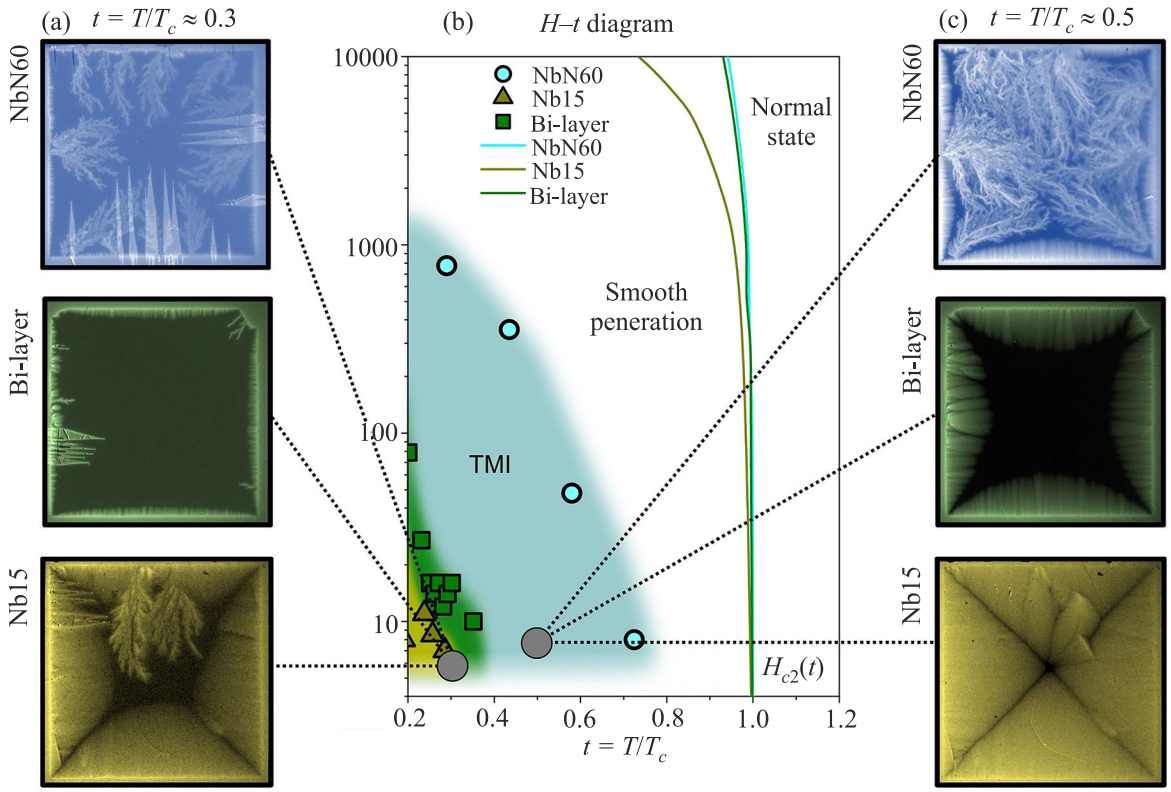

Fig. 4. (Color online) Column (a) shows MO images for each studied samples at $t \approx 0.3$ and $H = 4$ Oe. The zig-zag-like features in the images are related to domain walls in the indicator film. (b) *H–t* diagram showing the thermomagnetic instabilities regime (TMI) as a function of the reduced temperature; (c) MO images taken at $t \approx 0.5$ and $H = 8.5$ Oe.

history of the system. Fig. 5(a)–(e) presents quantitative MO images obtained at certain magnetic fields along the hysteresis loop of the NbN/Nb bilayer sample at $T = 3.5$ K. The spatial profile of the induction component $B_z(r)$ at the bottom of each image has been obtained from an average of 40 lines as shown by the translucent yellow bar in panel (a).

Figure 5(a) shows a typical critical state-like field profile for the virgin curve in a magnetization loop where the inner part of the film is still in the Meissner state (dark inner area), i.e., $B = 0$. In panel (b), the applied field reaches its maximum value ($H = 46$ Oe), and $B > 0$ at the center of the sample. The diagonal dark lines forming an X shape pattern are named discontinuity lines (d-lines), and delineate the locations where the supercurrent undergoes an abrupt change of direction. Panel (c) shows the flux density landscape after decreasing H down to 14 Oe starting from its maximum value, and just before the occurrence of the first anti-avalanche in the system. The field profile in panel (c) reveals a large quantity of positive flux trapped in the sample. The first anti-avalanche (d) starts from the top left corner into the positive upper left d-line. This preferential track suggests that most likely this avalanche is driven by the flux-antiflux annihilation process. The magnetic profile at the bottom of panel (d) shows the recorded imprint of this anti-avalanche, and it does not change the polarity of the induction field B along its path, but strongly decreases the local field as it passes. By decreasing the applied magnetic field by 1 Oe, another anti-avalanche is triggered from the left edge, transpassing the center of the sample and then crossing the first avalanche of anti-flux. The second anti-avalanche does not change the local field to negative values, although it decreases further the average B in the whole sample. Nevertheless, these two anti-avalanches exhibit particular features that can be better emphasized by implementing differential MOI [51], i.e., by subtracting consecutively recorded images. The result of this procedure is presented in panels (f) and (g) of Fig. 5.

Note that the first anti-avalanche running along the d-line produces end branches directed along the crossing

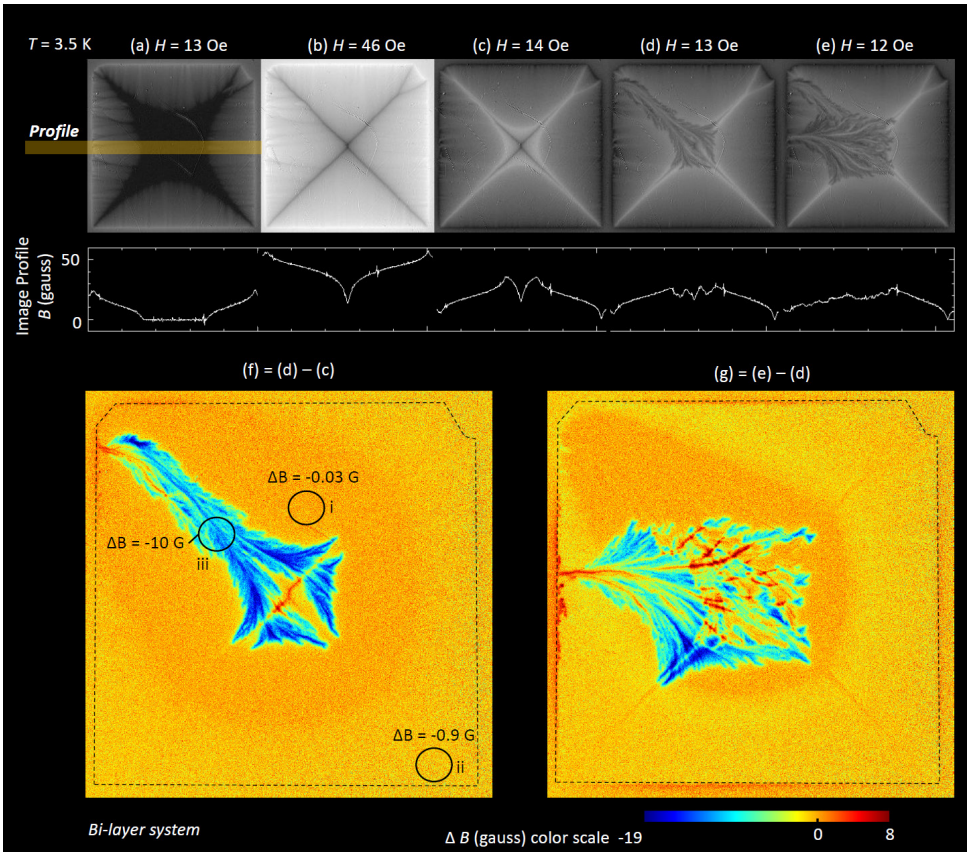

Fig. 5. (Color online) (a)–(e) A sequence of quantitative MO images of the bi-layer system, for different applied magnetic fields, after a ZFC procedure, at $T = 3.5$ K. At the bottom of each panel, the field profile is shown, averaged from 40 lines delimited by the translucid yellow bar identified in panel (a). (f) Differential image obtained by subtracting (d) and (c) panels, which shows the first anti-avalanche and an orange halo surrounding it. The field variation ΔB is indicated by black circles, (i) inside the halo, (ii) outside the halo, and (iii) inside the avalanche. (g) Differential image between panels (e) and (d), where the second anti-avalanche crosses the first one. The color scale indicates that the trapped field increased in some regions where the avalanche branches cross. The dashed lines in panels (f) and (g) are indications of the sample edges.

d-line. A remarkable feature is the appearance of a halo surrounding the anti-avalanche, a feature that, to the best of our knowledge, has not been reported so far. To describe this halo in a quantitative form, we measured the average variation of B in three circular regions with 25,000 pixels each in different regions throughout the sample. The result is marked by the black circles seen in panel (f). The circle (i), inside the halo itself, is the region where the local field decreased less ($\Delta B_i = -0.03$ G). This procedure was done in other points across the halo (not shown), to confirm this observation. Outside the halo, the circle (ii) results in $\Delta B_{ii} = -0.9$ G, and inside the avalanche (circle (iii)), the average flux density variation from this area was $\Delta B_{iii} = 16\text{ G} - 26\text{ G} = -10$ G. According to the color scale, one can see that there are regions in the anti-avalanche branches where the field variation is as high as –19 G. The differential MO image in panel (f) allows one to state that the average field in the sample decreased. The trapped flux in the system seems to lead to this unexpected halo. More details on the halo structure and its surroundings are provided in the next section. The sample Nb15 also shows a halo-like structure around its first anti-avalanche, but this halo was not detected in the film NbN60. The halo is not a thick annihilation zone, as one can see in the B profile of Fig. 5(d) and (e) — there is no crossover between positive to negative flux there, and thus, no zero-field region. This halo refers to the absence of rearrangement of the flux distribution in the region around the abrupt penetration during the first anti-avalanche.

Another intriguing aspect of this set of images is that the second anti-avalanche crosses the first one. The color scale in Fig. 5(g) allows one to highlight the fact that the branches of the first avalanche transpassed by the second one, undergo a positive variation of the local magnetic field as high as 8 G. Flux avalanches triggered during a ZFC procedure are known for avoiding each other during their propagation into the sample [15], no matter whether they are small and fingerlike or large and highly branched. However, avalanches may cross each other in descending fields because there is still a positive flux where the prior anti-avalanche passed. Although the halo of the first anti-avalanche has changed after the advent of the second avalanche, this last one does not have a halo surrounding it.

3.4. Halo definition

What we call halo is a region of extra brightness (in our case, ΔB) surrounding the first anti-avalanche for the bilayer system. Figure 6(a) is a differential image, as presented in Fig. 5(f). Panels (b), (c) and (d) are the averaged ΔB profiles for three regions of the sample, indicated by translucent gray bars. Panel (b) shows the ΔB profile passing through the avalanche trunk, where there is an intense negative variation of B ($\Delta B < 0$), as well as a smooth variation close to the sample edges (outside the halo). In (c), the halo region presents the highest brightness in the whole image ($\Delta B = 0$). Panel (d) presents a region outside the halo where ΔB is negative and constant. Therefore, the halo is suitable to describe such a region in the framework of differential images.

4. Conclusions

In this paper, we propose an approach to reduce the flux avalanche activity in NbN films by coating them with an Nb layer. This measure may improve the applicability of thin films of NbN without changing its upper critical field at the same reduced temperature. A similar effect has been reported when the superconductive film is coated with a normal metal [30,36,52–55]. The region where the avalanches take place in the field-reduced temperature diagram decreases for the hybrid system as compared to the

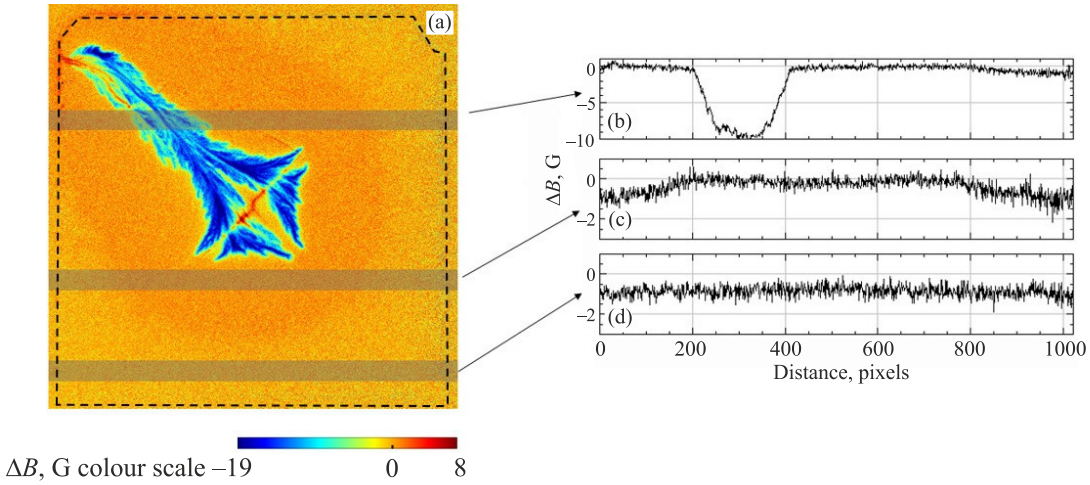

Fig. 6. (Color online) Description of the halo structure. (a) Differential image obtained by subtracting (d) and (c) panels of Fig. 5, presented as panel (f). Averaged ΔB profiles taken from the translucent gray bars, passing through (b) the anti-avalanche, (c) the halo, and (d) outside the halo.

single NbN layer, becoming closer to the single Nb film. In other words, there is a suppression of the occurrence of flux avalanches in the hybrid NbN/Nb system without considerably depreciating its other properties. In addition to that, quantitative MOI allows one to unveil anti-avalanches crossing, as well as the lack of vortex rearrangement in a large region surrounding the first anti-avalanche. This latter effect manifests itself as a halo of nearly unperturbed magnetic field intensity.

Acknowledgements

This work was partially supported by the National Council for Scientific and Technological Development (CNPq), by the Coordenção de Aperfeiçoamento de Pessoal de Nível Superior–Brasil (CAPES)–Finance Code 001, by the Brazilian program Science without Borders, and by the Norwegian Research Council. The authors thank the COST action NanoCoHybri (CA16218). AVS acknowledges support from the Fonds de la Recherche Scientifique — FNRS.

1. J. Bardeen and M.J. Stephen, *Phys. Rev. A* **140**, 1197 (1965).
2. W. Klein, R.P. Huebener, S. Gauss, and J. Parisi, *J. Low Temp. Phys*. **61**, 413 (1985).
3. A.I. Larkin and Yu.N. Ovchinnikov, *Sov. Phys. JETP* **41**, 960 (1976).
4. D.Y. Vodolazov and F.M. Peeters, *Phys. Rev. B* **76**, 014521 (2007).
5. A.V. Silhanek, M.V. Milošević, R.B.G. Kramer, G.R. Berdiyorov, J. Van de Vondel, R.F. Luccas, T. Puig, F.M. Peeters, and V.V. Moshchalkov, *Phys. Rev. Lett*. **104**, 017001 (2010).
6. L. Embon, Y. Anahory, Ž.L. Jelić, E.O. Lachman, Y. Myasoedov, M.E. Huber, G.P. Mikitik, A.V. Silhanek, M.V. Milošević, A. Gurevich, and E. Zeldov, *Nature Commun*. **8**, 85 (2017).
7. A. Andronov, I. Gordion, V. Kurin, I. Nefedov, and I. Shereshevsky, *Physica C* **213**, 193 (1993).
8. A.I. Bezuglyj and V.A. Shklovskij, *Physica C* **202**, 234 (1992).
9. A.I. Bezuglyj, V.A. Shklovskij, R.V. Vovk, V.M. Bevz, M. Huth, and O.V. Dobrovolskiy, *Phys. Rev. B* **99**, 174518 (2019).
10. E.H. Brandt, *Rep. Progr. Phys*. **58**, 1465 (1995).
11. A.V. Bobyl, D.V. Shantsev, T.H. Johansen, W.N. Kang, H.J. Kim, E.M. Choi, and S.I. Lee, *Appl. Phys. Lett*. **80**, 4588 (2002).
12. D. Carmo, F. Colauto, A.M.H. de Andrade, A.A.M. Oliveira, W.A. Ortiz, and T.H. Johansen, *Supercond. Sci. Technol.* **29**, 095003 (2016).
13. E. Altshuler and T.H. Johansen, *Rev. Mod. Phys*. **76**, 471 (2004).
14. I.S. Aranson, A. Gurevich, M.S. Welling, R.J. Wijngaarden, V.K. Vlasko-Vlasov, V.M. Vinokur, and U. Welp, *Phys. Rev. Lett.* **94**, 037002 (2005).
15. T.H. Johansen, M. Baziljevich, D.V. Shantsev, P.E. Goa, Y.M. Galperin, W.N. Kang, H.J. Kim, E.M. Choi, M.-S. Kim, and S.I. Lee, *Supercond. Sci. Technol.* **14**, 726 (2001).
16. I. Aranson, A. Gurevich, and V. Vinokur, *Phys. Rev. Lett.* **87**, 067003 (2001).
17. D.V. Denisov, A.L. Rakhmanov, D.V. Shantsev, Y.M. Galperin, and T.H. Johansen, *Phys. Rev. B* **73**, 014512 (2006).
18. D.V. Denisov, D.V. Shantsev, Y.M. Galperin, E.M. Choi, H.S. Lee, S.I. Lee, A.V. Bobyl, P.E. Goa, A.A.F. Olsen, and T.H. Johansen, *Phys. Rev. Lett.* **97**, 077002 (2006).
19. E.M. Choi, H.S. Lee, J.Y. Lee, S.I. Lee, Å.A.F. Olsen, V.V. Yurchenko, D.V. Shantsev, T.H. Johansen, H.J. Kim, and M.H. Cho, *Appl. Phys. Lett.* **91**, 042507 (2007).
20. V.V. Yurchenko, D.V. Shantsev, T.H. Johansen, M.R. Nevala, I.J. Maasilta, K. Senapati, and R.C. Budhani, *Phys. Rev. B* **76**, 092504 (2007).
21. F. Colauto, E.J. Patiño, M.G. Blamire, and W.A. Ortiz, *Supercond. Sci. Technol.* **21**, 045018 (2008).
22. I.A. Rudnev, D.V. Shantsev, T.H. Johansen, and A.E. Primenko, *Appl. Phys. Lett.* **87**, 1 (2005).
23. M. Ashkin, J.R. Gavaler, J. Greggi, and M. Decroux, *J. Appl. Phys*. **55**, 1044 (1984).
24. D. Hazra, N. Tsavdaris, S. Jebari, A. Grimm, F. Blanchet, F. Mercier, E. Blanquet, C. Chapelier, and M. Hofheinz, *Supercond. Sci. Technol.* **29**, 105011 (2016).
25. I. Tretyakov, S. Ryabchun, M. Finkel, A. Maslennikova, K. Natalia, A. Lobastova, B. Voronov, and G. Gol'tsman, *Appl. Phys. Lett.* **98**, 033507 (2011).
26. V. Michal, S. Bouat, J. Villegier, and J. Sedlacek, *Superconducting NbN Band-pass Filter and Matching Circuit for 30 GHz RSFQ Data Converter*, in: *2009, 19th International Conf. Radioelektron*. (2009), p. 161.
27. V. Larrey, J. Villegier, M. Salez, F. Miletto-Granozio, and A. Karpov, *IEEE Transact. Appl. Supercon*. **9**, 3216 (1999).
28. R. Cheng, C.-L. Zou, X. Guo, S. Wang, X. Han, and H.X. Tang, *Nature Commun*. **10**, 4104 (2019).
29. W. Qiu, K. Makise, H. Terai, Y. Nakamura, and Z. Wang, *J. Phys.: Confer. Ser*. **507**, 042032 (2014).
30. V.V. Yurchenko, A.J. Qviller, S. Chaudhuri, I.J. Maasilta, D. V. Shantsev, Y.M. Galperin, and T.H. Johansen, *Suppression of Magnetic Flux Avalanches and Recovery of the Critical State in Superconducting NbN Films* (2012).
31. P. Fabbricatore, M. Greco, C. Ferdeghini, C. Bernini, U. Gambardella, G. Celentano, and A. Devred, *Supercond. Sci. Technol.* **20**, 2 (2007).
32. S.V. Vasiliev, O. M. Chumak, V.V. Chabanenko, F. Pérez-Rodríguez, and A. Nabiałek, *Acta Phys. Polonica A* **126**, A84 (2014).
33. O.M. Chumak, V.V. Chabanenko, V.F. Rusakov, S.V. Vasiliev, F. Pérez-Rodríguez, and A. Nabiałek, *J. Low Temp. Phys*. **179**, 75 (2015).
34. Y. Ivry, J.J. Surick, M. Barzilay, C.-S. Kim, F. Najafi, E. Kalfon-Cohen, A.D. Dane, and K.K. Berggren, *Nanotechnology* **28**, Art. No. 435205 (2017).

35. T. Tamegai, A. Mine, Y. Tsuchiya, S. Miyano, S. Pyon, Y. Mawatari, and S. Nagasawa, *Physica C* **533**, 74 (2017).
36. J. Brisbois, V.N. Gladilin, J. Tempere, J.T. Devreese, V.V. Moshchalkov, F. Colauto, M. Motta, T.H. Johansen, J. Fritzsche, O.-A. Adami, N.D. Nguyen, W.A. Ortiz, R.B.G. Kramer, and A.V. Silhanek, *Phys. Rev. B* **95**, 094506 (2017).
37. Ch. Jooss, J. Albrecht, H. Kuhn, S. Leonhardt, and H. Kronmüller, *Rep. Progr. Phys*. **65**, 651 (2002).
38. L.E. Helseth, R.W. Hansen, E.I. Il'yashenko, M. Baziljevich, and T.H. Johansen, *Phys. Rev. B* **64**, 174406 (2001).
39. F. Colauto, M. Motta, A. Palau, M.G. Blamire, T.H. Johansen, and W.A. Ortiz, *IEEE Transact. Appl. Supercond.* **25**, Art. No. 7500704 (2015).
40. L.E. Helseth, A.G. Solovyev, R.W. Hansen, E.I. Il'yashenko, M. Baziljevich, and T.H. Johansen, *Phys. Rev. B* **66**, 064405 (2002).
41. G. Shaw, J. Brisbois, L.B.G.L. Pinheiro, J. Müller, S. Blanco Alvarez, T. Devillers, N.M. Dempsey, J.E. Scheerder, J. Van De Vondel, S. Melinte, P. Vanderbemden, M. Motta, W.A. Ortiz, K. Hasselbach, R.B.G. Kramer, and A.V. Silhanek, *Rev. Sci. Instrum.* **89**, 0213705 (2018).
42. M. Faucher, T. Fournier, B. Pannetier, C. Thirion, W. Wernsdorfer, J.C. Villegier, and V. Bouchiat, *Physica C* **368**, 211 (2002).
43. J.R. Gavaler, M.A. Janocko, A. Patterson, and C.K. Jones, *J. Appl. Phys*. **42**, 54 (1971).
44. J.H. Tyan and J.T. Lue, *J. Appl. Phys*. **75**, 325 (1994).
45. I. Giaever and K. Megerle, *Phys. Rev*. **122**, 1101 (1961).
46. A.V. Silhanek, S. Raedts, and V.V. Moshchalkov, *Phys. Rev. B* **70**, 144504 (2004).
47. M. Motta, F. Colauto, R. Zadorosny, T.H. Johansen, R.B. Dinner, M.G. Blamire, G.W. Ataklti, V.V. Moshchalkov, A.V. Silhanek, and W.A. Ortiz, *Phys. Rev. B* **84**, 214529 (2011).
48. R. Mints and A. Rakhmanov, *Rev. Mod. Phys*. **53**, 551 (1981).
49. C.P. Bean, *Phys. Rev. Lett*. **8**, 250 (1962).
50. E. Baruch-El, M. Baziljevich, T.H. Johansen, and Y. Yeshurun, *J. Supercond. Novel Magnet*. **28**, 379 (2015).
51. A. Soibel, E. Zeldov, M. Rappaport, Y. Myasoedov, T. Tamegai, S. Ooi, M. Konczykowski, and V.B. Geshkenbein, *Nature* **406**, 282 (2000).
52. E.M. Choi, H.S. Lee, H.J. Kim, B. Kang, S.I. Lee, A.A.F. Olsen, D.V. Shantsev, and T.H. Johansen. *Appl. Phys. Lett.* **87**, 152501 (2005).
53. J. Albrecht, A.T. Matveev, M. Djupmyr, G. Schütz, B. Stuhlhofer, and H.-U. Habermeier, *Appl. Phys. Lett.* **87**, 182501 (2005).
54. P. Mikheenko, A.J. Qviller, J.I. Vestgården, S. Chaudhuri, I.J. Maasilta, Y.M. Galperin, and T.H. Johansen, *Appl. Phys. Lett.* **102**, 022601 (2013).
55. J. Brisbois, B. Vanderheyden, F. Colauto, M. Motta, W.A. Ortiz, J. Fritzsche, N.D. Nguyen, B. Hackens, O.-A. Adami, and A.V. Silhanek, *New J. Phys*. **16**, 103003 (2014).

Лавини магнітного потоку у тонких плівках Nb/NbN

L.B.L.G. Pinheiro, M. Caputo, C. Cirillo, C. Attanasio, T.H. Johansen, W.A. Ortiz, A.V. Silhanek, M. Motta

Перспективи технологічного застосування тонких плівок NbN можуть опинитися під загрозою через розвиток лавин магнітного потоку термомагнітного походження, що виникають в значній частині надпровідної фази. У даній роботі описано підхід, який дозволяє істотно подавити лавинний режим магнітного потоку та не ставить під загрозу верхнє критичне поле. Ця процедура полягає в попередньому нанесенні тонкого шару Nb ще до реактивного осадження плівки NbN, в результаті чого утворюється двошарова система. Використано методи ac сприйнятливості та dc магнітометрії для отримання магнітних характеристик як одношарових плівок Nb та NbN, так і для двошарового зразка Nb / NbN, а також метод каліброваної магнітооптичної візуалізації для відображення просторового розподілу режиму нестабільності у досліджених зразках. Магнітна візуалізація потоку виявила цікаві особливості формування лавин дендритного потоку у двошаровій системі, зокрема наявність галоподібних структур та перетину лавин.

Ключові слова: двошарова система, ефект близькості, антилавина, галоподібна структура, перетин лавин.

Лавины магнитного потока в тонких пленках Nb/NbN

L.B.L.G. Pinheiro, M. Caputo, C. Cirillo, C. Attanasio, T.H. Johansen, W.A. Ortiz, A.V. Silhanek, M. Motta

Перспективы технологического применения тонких пленок NbN могут оказаться под угрозой из-за развития лавин магнитного потока термомагнитного происхождения, возникающих в значительной части сверхпроводящей фазы. В настоящей работе описан подход, позволяющий существенно подавить лавинный режим магнитного потока, не ставя под угрозу верхнее критическое поле. Эта процедура состоит в предварительном нанесении тонкого слоя Nb до реактивного осаждения пленки NbN, в результате чего образуется двухслойная система. Использованы методы ac восприимчивости и dc магнитометрии для получения магнитных характеристик как однослойных пленок Nb и NbN, так и для двухслойного образца Nb/NbN, а также метод калиброванной магнитооптической визуализации для отображения пространственного распределения режима нестабильности в исследуемых образцах. Магнитная визуализация потока выявила интересные особенности формирования лавин дендритного потока в двухслойной системе, в том числе наличие галообразных структур и пересечения лавин.

Ключевые слова: двухслойная система, эффект близости, антилавина, галообразная структура, пересечение лавин.